# In situ Observations of Catalyst Dynamics during Surface-Bound Carbon Nanotube Nucleation

Stephan Hofmann,*,[†] Renu Sharma,[‡] Caterina Ducati,[§] Gaohui Du,[‡]
Cecilia Mattevi,[⊥,#] Cinzia Cepek,[#] Mirco Cantoro,[†] Simone Pisana,[†] Atlus Parvez,[†]
Felipe Cervantes-Sodi,[†] Andrea C. Ferrari,[†] Rafal Dunin-Borkowski,[§,||]
Silvano Lizzit,[⊗] Luca Petaccia,[⊗] Andrea Goldoni,[⊗] and John Robertson[†]

*Department of Engineering, University of Cambridge, Cambridge CB3 0FA, UK, Center for Solid State Science, Arizona State University, Tempe, Arizona 85287-1704, Department of Materials Science and Metallurgy, University of Cambridge, Cambridge CB2 3QZ, UK, Center for Electron Nanoscopy, Technical University of Denmark, DK-2800 Kongens Lyngby, Denmark, University of Padova, Dipartimento di Scienze Chimiche, Via Marzolo no. 1, I-335131 Padova, Italy, Laboratorio Nazionale, TASC-CNR-INFM, s.s. 14, Km. 163.5, I-34012 Trieste, Italy, and Surface Science Division, Sincrotrone Trieste S.C.p.A., s.s. 14, Km. 163.5, I-34012 Trieste, Italy*

Received October 23, 2006; Revised Manuscript Received February 5, 2007

## ABSTRACT

We present atomic-scale, video-rate environmental transmission electron microscopy and in situ time-resolved X-ray photoelectron spectroscopy of surface-bound catalytic chemical vapor deposition of single-walled carbon nanotubes and nanofibers. We observe that transition metal catalyst nanoparticles on $SiO_x$ support show crystalline lattice fringe contrast and high deformability before and during nanotube formation. A single-walled carbon nanotube nucleates by lift-off of a carbon cap. Cap stabilization and nanotube growth involve the dynamic reshaping of the catalyst nanocrystal itself. For a carbon nanofiber, the graphene layer stacking is determined by the successive elongation and contraction of the catalyst nanoparticle at its tip.

The unique electronic, mechanical, and optical properties of carbon nanotubes (CNTs) relate closely to their atomic structure. Single-walled carbon nanotubes (SWNTs) are fully defined by their diameter and chiral angle, which determines whether the tube is a metal or semiconductor and its band gap. The properties of multi-walled carbon nanotubes (MWNTs) and carbon nanofibers (CNFs) depend on the number of walls and the graphene layer stacking, respectively. However, at present, neither SWNT chirality nor the structure of a CNF can be controlled sufficiently during growth despite the development of a wide range of synthesis techniques. This is due to an incomplete understanding of the role of the catalyst in nanotube nucleation and growth.

Existing models of catalytic nucleation rely heavily on the quality of direct experimental observation. SWNT nucleation during high-temperature arc-discharge and laser ablation processes is difficult to monitor in situ.[1] Most evidence for SWNT formation from condensed catalyst particles arises from post-growth high-resolution transmission electron microscopy (HRTEM).[2] Presently, chemical vapor deposition (CVD) is increasingly important for applications[3] because it allows the controlled, selective growth of CNTs directly on a substrate as well as bulk production.[4] Surface-bound CVD enables the direct observation of the catalytic nucleation process at the atomic scale.[5,6] Previous ex situ characterization of CVD growth suggests that a CNT grows by carbon extrusion,[7,8] i.e., that CNT growth is fed solely via the catalyst particle interface. Post-growth HRTEM analysis typically finds the SWNT wall aligned tangential to the catalyst cluster, whereby the catalyst particle appears to have dictated the tube diameter.[9,10] However, such post-growth characterization is static and can be ambiguous due to changes during cooling and transfer. This leaves key questions such as how the nanotubes nucleate and whether the catalyst is liquid or solid difficult to answer.

* Corresponding author. E-mail: sh315@cam.ac.uk.
[†] Department of Engineering, University of Cambridge.
[‡] Center for Solid State Science, Arizona State University.
[§] Department of Materials Science and Metallurgy, University of Cambridge.
[||] Center for Electron Nanoscopy, Technical University of Denmark.
[⊥] University of Padova, Dipartimento di Scienze Chimiche.
[#] Laboratorio Nazionale, TASC -CNR-INFM.
[⊗] Surface Science Division, Sincrotrone Trieste S.C.p.A.

Here, we present atomic-scale environmental TEM (ETEM) and in situ time-resolved X-ray photoelectron spectroscopy (XPS) of dynamic effects before and during catalyst-assisted CVD of CNFs and SWNTs. We focus on acetylene decomposition over $SiO_x$-supported Ni and Fe catalyst films. It is important that the gases and pressures during ETEM observations are similar to those used in our normal CVD experiments[11,12] so that we can draw realistic conclusions about what determines structural selectivity.

We used a modified Tecnai F20 ETEM, operated at 200 kV, equipped with a differential pumping system and a Gatan imaging filter.[13] The microscope permits pressures of up to 10 mbar, with a specified information limit of 0.14 nm. Video sequences can be recorded with 30 frames/s time resolution. The electron dose was representative of that typically implemented for high-resolution imaging,[14] and the electron beam was never focused onto the specimen in order to minimize the effects of electron-beam-induced damage and modification of the specimen. Thin catalyst films (99.9% purity) were thermally evaporated (base pressure $\sim 10^{-6}$ mbar) onto perforated $SiO_x$ membranes (SPI supplies) or onto 2000 mesh Cu TEM grids (Agar Scientific) coated with $SiO_x$ nanopowder (Degussa Aerosil Ox50) and a $\sim 30$ nm sputtered $SiO_x$ layer. The samples were transferred in air to the ETEM.

In situ time-resolved XPS was carried out in the ultrahigh vacuum (UHV) end-station of the SuperESCA beamline (base pressure $< 1 \times 10^{-10}$ mbar) at the Elettra Synchrotron. A high flux of $100-400$ eV photons allowed core-level spectra to be acquired within $\sim 5$ s with an energy resolution below 80 meV. The probe size was 30 $\mu$m $\times$ 200 $\mu$m. Fe and Ni catalyst films of 99.9% purity were deposited in situ on polished Si(100) substrates covered with 150 nm thermally grown $SiO_2$. Acetylene was introduced using a gas-doser with a microchannel plate head. During the measurements, the distance from the microchannel plate head to the sample was 15 mm. This setup allows direct measurements in gas background pressures up to $10^{-6}$ mbar. Higher pressure exposures were carried out in a prechamber. The samples were also characterized ex situ by field emission gun scanning electron microscopy (SEM, LEO 1530VP FEG-SEM), HRTEM (JEOL JEM 4000EX, 400 kV; Tecnai F20, 200 kV), and Raman spectroscopy (Renishaw 1000 Raman spectrometer, 514, 633, and 785 nm excitation).

The overall CVD growth process consists of two steps, a catalyst pretreatment step followed by a nanotube growth step.[12] In step 1, the initial thin film catalyst is transformed by dewetting from the $SiO_x$ into a series of isolated nanoparticles (Figure 1). It is known that dewetting initiates at grain boundaries and edges through surface diffusion and that the metal thereby can remain crystalline.[15,16] The film restructuring, further sintering, and the crystal shape[17] reflect a surface and interface energy minimization. A reactive ambient can change the chemical state of the catalyst and influence its shape via adsorbate-induced changes of surface energies and changes of the interfacial energy,[17] hence the catalyst particle shape and size distribution are related intimately to the CVD conditions used.[18,19]
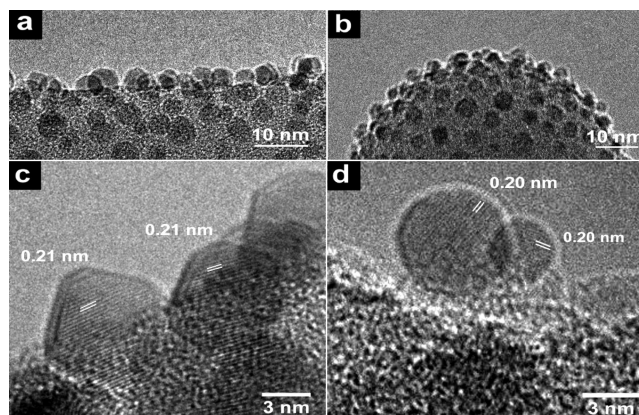


**Figure 1.** ETEM images of an initially (partially) oxidized 1 nm Ni film recorded at (a,c) 480 °C in 1 mbar $NH_3$ on an $SiO_x$ membrane, (b) 450 °C, and (d) 615 °C in vacuum ($10^{-6}$ mbar) on an $SiO_x$-covered silica nanoparticle.

HRTEM analysis shows that Ni (Figure 1) and Fe (Figure 2a,b) nanoparticles are crystalline during the pretreatment step before CNF (Figure 1a,c) and SWNT growth (Figure 1b,d). A nominally 1 nm thick catalyst film typically transforms into an island size distribution centered around 5 nm,[18,20] which is broadened considerably here by the non-planarity of the TEM-compatible substrates. For most nanocrystals, only one set of lattice fringes is visible, which can make the analysis of their chemical state solely based on lattice assignments ambiguous. The 0.20 nm reflection is expected for metallic fcc Ni(111), but also for $Ni_2O_3$(200) and $Ni_3C$(113). We therefore include XPS measurements, in particular to follow changes in the chemistry related to the particle surfaces. It should be noted that the initial Ni films were (partially) oxidized due to transfer in air. It appears that some of the Ni nanocrystals that are held at 480 °C in $NH_3$ are still oxidized, as the 0.21 $\pm$ 0.01 nm spacing can best be assigned to (200) lattice planes in NiO (0.208 nm) (Figure 1c). This observation would also be consistent with the faceting, although we cannot comment on $NH_3$-induced restructuring. In addition, measurements of lattice spacings from nanocrystals may be affected both by their finite size and rapid variation in thickness and by variations in their orientation.[21]

XPS reveals that the Fe and Ni 3p core levels (not shown) of UHV-deposited Fe and Ni remain metallic during the pretreatment step. That is, in situ evaporated metal catalyst on $SiO_2$ remains unoxidized. It was previously shown that oxidized Fe is reduced by acetylene exposure during nanotube CVD.[22] The catalyst is active in its metallic state; Fe and Ni films that were deliberately oxidized before annealing showed a lower nanotube yield at direct $C_2H_2$ exposure.[23]

We now turn to the XPS analysis of the CNT growth step. Nanotubes were nucleated by exposing nominally 0.5 nm thick Fe films to undiluted $C_2H_2$ at 580 °C. Figure 2c shows the evolution of the C 1s core level spectrum during acetylene exposure at a background pressure of $\sim 2 \times 10^{-7}$ mbar $C_2H_2$. The appearance of a peak at $\sim 282.6$ eV precedes an intermediate peak at $\sim 283.2$ eV and the increase of a very strong peak at $\sim 284.5$ eV, which saturates after $\sim 150$ s
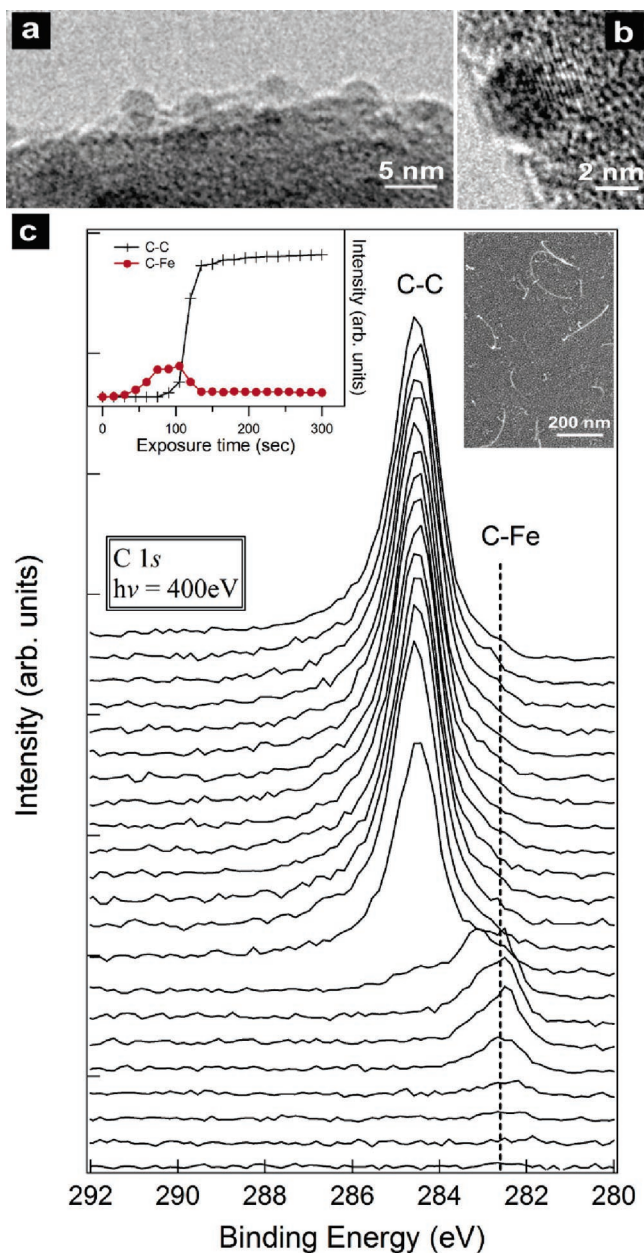
**Figure 2.** (a,b) ETEM images of an initially oxidized 0.3 nm Fe film at 480 °C in 1 mbar $NH_3$ on an $SiO_x$-covered silica nanoparticle. (c) Time-resolved evolution of C 1s core level during Fe exposure to $\sim 2 \times 10^{-7}$ mbar (background pressure) $C_2H_2$ at 580 °C. Insets show an SEM image of part of the probed area and the time-evolution of the chemisorbed (dots) and graphitic (crosses) carbon peaks.
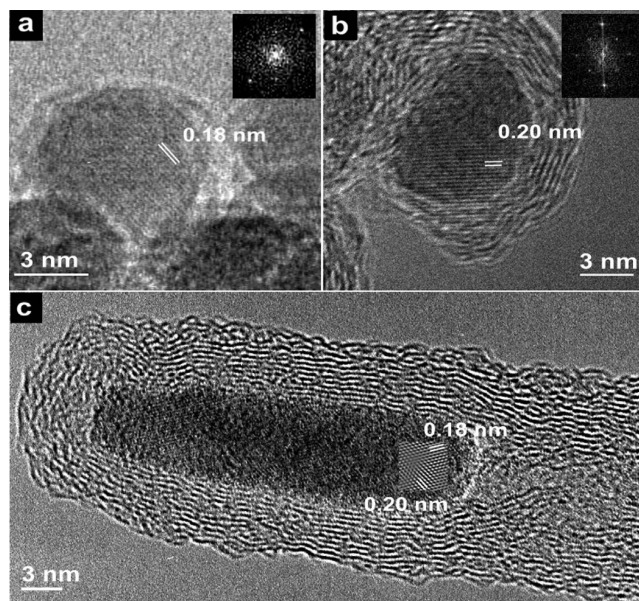


**Figure 3.** ETEM images of Ni nanocrystals recorded at (a) 480 °C and (b) 360 °C in 3:1 $NH_3$:$C_2H_2$ at 1.3 mbar total pressure. The insets show FFTs of the respective particles. (c) HRTEM image of the tip region of a Ni-catalyzed CNF grown ex situ at 700 °C in 2.7:1 $NH_3$:$C_2H_2$ at 5.2 mbar total pressure. The fcc Ni particle is imaged in the [110] projection. The inset shows a Fourier-filtered image of the lattice.

(Figure 2c, inset). We interpret this chemical shift in the C 1s binding energy as a transition from chemisorbed carbon ($\sim 282.6$ eV)[24] to carbidic carbon ($\sim 283.2$ eV)[25] and to an $sp^2$-bonded carbon network ($\sim 284.5$ eV).[26] The C−C bond starts to appear after $\sim 90$ s of acetylene exposure at the saturation of the chemisorbed signal. It should be emphasized that the XPS signal represents a spatial average over the accessible catalyst particle surface in the beam area, wherein not all catalyst particles nucleated a CNT (Figure 2c, inset). At the conditions used here, the XPS information depth is $\sim 0.5$ nm, hence the attenuation of the chemisorbed peak in

Figure 2c may result from increased carbon network formation. We could not detect a carbon signal on the plain $SiO_2$ substrate under our conditions, indicating a highly selective $C_2H_2$ decomposition on the metal catalyst (Figure 2).[11]

The XPS data does not allow a distinction between surface carbide[27] (carbon-rich (sub)surface layer) and bulk catalyst carbide formation.[22] It is interesting to note that the time evolution observed for the chemisorbed and graphitic C peaks (Figure 2c, inset) is similar to reported SWNT incubation times extrapolated for low-pressure $C_2H_2$ exposure of Ni.[6] We also note that in the latter study electron diffraction indicated the absence of bulk $Ni_3C$ during SWNT growth.[6] Carbidic carbon has been reported previously as the single remaining species following temperature-programmed $C_2H_2$ and $C_2H_4$ decomposition on Ni.[28] Despite the (at present) limited overlap between our XPS and ETEM data, we stress that the selective feed stock decomposition and the formation of a carbon-rich (sub)surface layer are an integral part of catalyst dynamics during CNT growth.

ETEM shows that the core of a Ni catalyst nanoparticle remains crystalline during the continuous exothermic $C_2H_2$ dissociation and carbon network formation (Figure 3). The 0.18 nm lattice spacing observed in Figure 3a can be assigned to (200) lattice planes in metallic Ni. During CNF nucleation, the catalyst particle transforms from its initial equilibrium shape (Figure 1c) into a highly elongated shape. ETEM videos show that the Ni particle elongates until it suddenly contracts into a rounder shape, and the sequence recurs (Figure 4 and Supporting Information video S1). Typically, the substrate anchorage is overcome during the first contraction and the catalyst crystal lifts off the substrate, resulting in a tip growth mode.
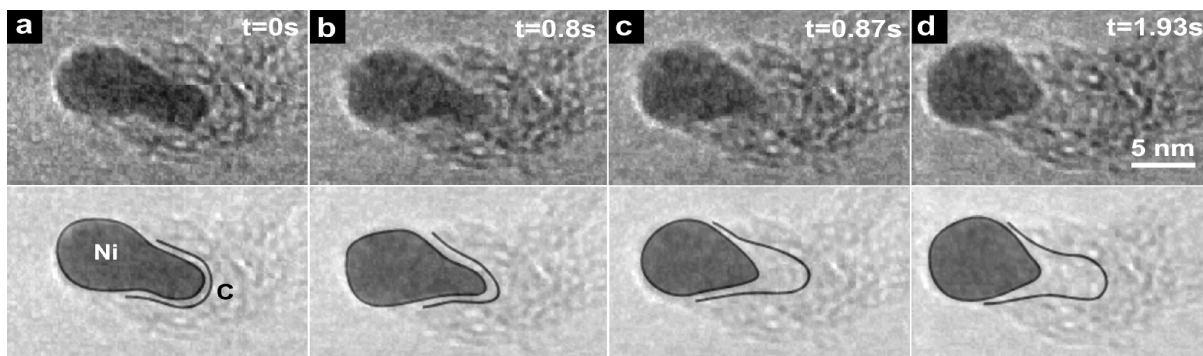
**Figure 4.** (a−d) ETEM image sequence showing a growing CNF in 3:1 NH$_3$:C$_2$H$_2$ at 1.3 mbar and 480 °C. The video was recorded at 30 frames/s, and the time of the respective stills is indicated. Drawings (lower row) indicate schematically the Ni catalyst deformation and C−Ni interface.
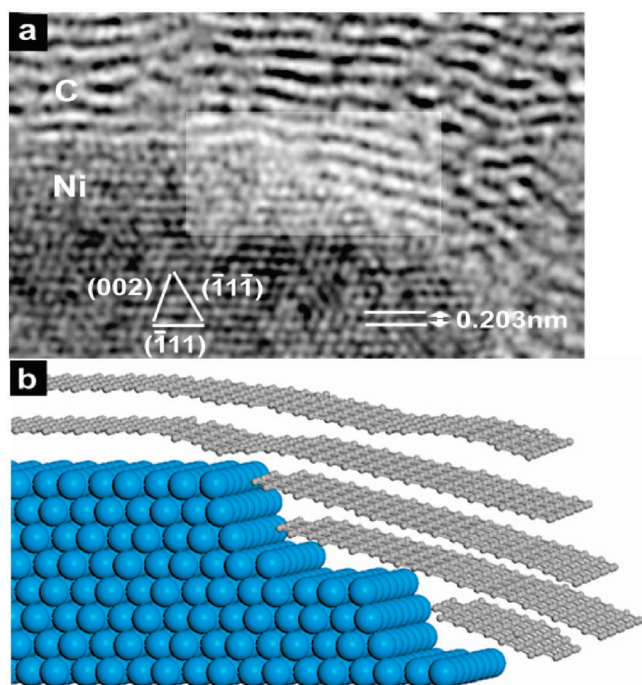


**Figure 5.** (a) HRTEM image of Ni−C interface at the tip of a CNF grown ex situ at 700 °C in 2.7:1 NH$_3$:C$_2$H$_2$ at 5.2 mbar total pressure. The principal planes of the Ni crystal in the [110] projection are indicated. (b) Schematic ball-and-stick model of area highlighted in (a).

The Ni catalyst behaves in an apparent "liquidlike" fashion analogous to the observations for solid-state dewetting (Figure 1).[16] In this context, "liquidlike" denotes that the Ni exhibits fast self-diffusivity but shows long-range crystalline order, in contrast to real liquids. Dynamic coexistence is typically observed for nanoparticles less than 2 nm in size,[29] thus mainly relevant for small-diameter SWNT nucleation. Fluctuating Bragg contrast due to Ni crystallinity is apparent in Supporting Information video S1.

Carbon layers terminate at a stepped Ni surface, which is analyzed in more detail in Figure 5a. The Ni fcc lattice is seen in a [110] projection. The corresponding ball-and-stick model (Figure 5b) shows Ni steps 3−4 monolayers in height, with graphitic layers emerging at various angles. Subsequent graphitic layers nucleate at an already-grown Ni−C interface

(Supporting Information video S1). Such C-stabilized Ni step-edges are often not in direct contact with the CVD atmosphere, i.e., are not at the same time the active sites for C$_2$H$_2$ dissociation. Thus the process involves diffusion of C atoms toward and Ni atoms away from the graphitic layer−Ni interface.[5] This Ni flux contributes to the observed elongation of the Ni catalyst crystal (Supporting Information video S1).

The dynamics of the Ni crystal reshaping are essential for the alignment of the graphitic layers into a CNF rather than a carbon onion (Figure 3b). For a bamboo-structured CNF, the Ni particle elongation is followed by an abrupt contraction, which leaves a conformal carbon overcoat behind and thereby creates the characteristic bamboolike intersects (Figure 4 and Supporting Information video S1). The time at which a contraction occurs has been attributed to the point at which the increase in Ni surface energy can no longer be compensated by the energy gain of binding the graphitic fiber to the Ni surface.[5] A more continuous elongation/contraction of a catalyst particle with a wedge-shaped tail will lead to a herringbone-like CNF crystallinity. A tangential extrusion of graphene layers without the carbon (re)coating of the catalyst particle tail will result in the formation of a hollow MWNT. An analysis of such dynamical behavior at the nanoscale requires further modeling, as many bulk properties appear to distinctively change. We also find that splitting of the catalyst particle can lead to CNF branching or to encapsulation of catalyst metal along the CNF body (data not shown).

For the given CNF CVD conditions, defect incorporation and disordering are frequently observed. The carbon arrival rate appears to be too high compared to the defect repair rate to effectively anneal out defects while they are still near the growth front. The resulting defective C network in turn influences the catalyst particle dynamics, possibly leading to a further propagation of defects in the growing CNF structure (Supporting Information video S1). It should be noted that the stepped Ni−C interface (Figure 5) can extend asymmetrically around the Ni particle, leading to incomplete closure of graphitic C sheets.[5] As it is known from HOPG,[30] open-ended graphene layers are stable during formation if the carbon dangling bonds can be saturated, e.g., by hydrogen.
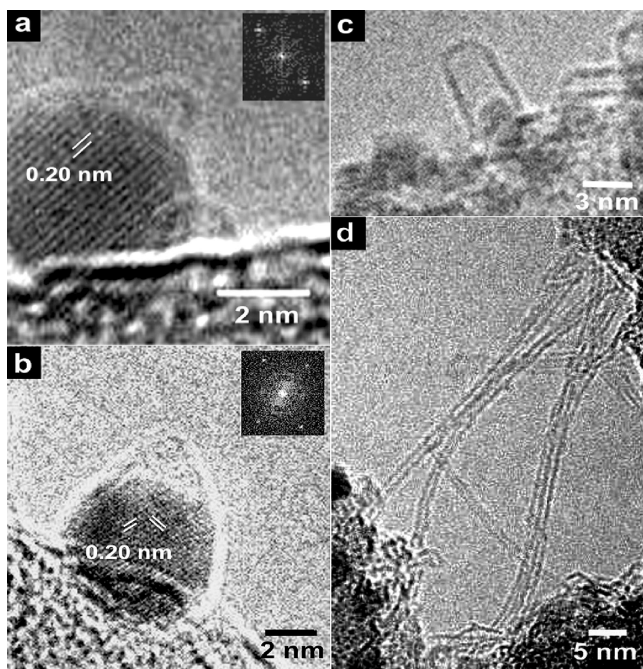
**Figure 6.** (a,b) ETEM images of Ni nanocrystals (Figure 1d) recorded at 615 °C in $8 \times 10^{-3}$ mbar $C_2H_2$. The insets show FFTs of the respective particles. (c,d) Ex situ HRTEM images acquired from the same samples.

Electron energy loss spectroscopy (EELS) shows nitrogen incorporation for CNFs grown in $NH_3$ (data not shown). This suggests that the role of reactive CVD gases has to be discussed in terms of changes to the chemical state of the catalyst particle and its surface energy combined with the effects on feedstock dissociation, carbon diffusion, and graphitic C formation. It is obvious that most of these processes are pressure and temperature dependent. Carbon activity drives the dynamic restructuring of the catalyst, which determines structural selectivity. CNT growth ceases when the reciprocal Ni−C interaction is interrupted, i.e., when catalyst particle elongation is suppressed and the Ni surface becomes encapsulated by carbon.

Figures 6 and 7 show ETEM and HRTEM data of various stages of SWNT growth. In contrast to CNF nucleation conditions, we anneal the 1 nm thick Ni film in vacuum to ~615 °C (Figure 1d) and expose it to undiluted $C_2H_2$ at lower pressures. The ETEM images in Figure 6a,b show Ni crystals for which SWNT nucleation has stopped early. A small-sized carbon cap has emerged on top of each catalyst particle. The carbon network surrounding the deactivated Ni particle forces a stronger faceting. Clear crystalline lattice fringe contrast is visible in the Ni clusters held at ~615°C. We assign the strong reflections in the FFT of Figure 6b to {111} planes, with the fcc Ni lattice oriented close to the [110] axis. Ex situ HRTEM imaging of SWNTs at a more progressed stage of growth shows the graphitic lattice of a hemispherically capped tube oriented tangentially to the catalyst cluster (Figure 6c), which is a very common observation[9] despite larger diameter SWNTs reportedly tending to have cone-shaped caps.[10]

Parts a−c of Figure 7 show an ETEM image sequence extracted from Supporting Information video S2. We believe that this sequence is representative of SWNT base growth, even though the nanotube is defective and growth terminates quickly. The Ni catalyst crystal strongly reshapes on its $SiO_x$ support, which explains the previous static observations of the various growth stages (Figure 6). Initially, a carbon cap emerges with a diameter smaller than the catalyst cluster. The carbon cap appears to replicate the shape of the apex of the triangular/pyramidal metal particle. The carbon network expands by lifting off from the catalyst particle, which itself is thereby restructured. The growing nanotube forces its shape onto the Ni cluster. The contact angle of the Ni particle to the $SiO_x$ substrate increases to approximately 90°, whereby the nanotube constrains the Ni particle to a more cylindrical shape. Growth terminates when the tangential graphitic lattice encapsulates the catalyst particle down to its support inter-face. The highly idealized ball-and-stick models shown in Figure 7d−f summarize the different SWNT growth stages.

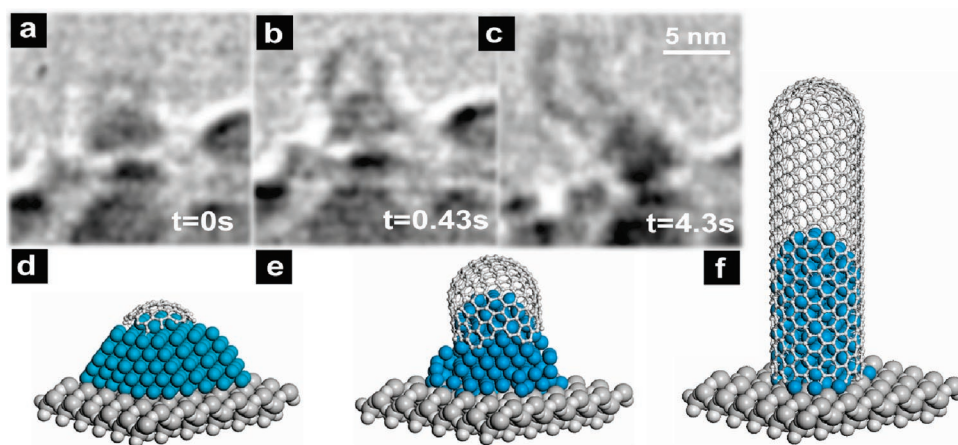It has been previously suggested that step sites on the catalyst surface nucleate the graphitic lattice formation[5] and



**Figure 7.** (a−c) ETEM image sequence of Ni-catalyzed CNT root growth recorded in $8 \times 10^{-3}$ mbar $C_2H_2$ at 615 °C (extracted from Supporting Information video S2). The time of the respective stills is indicated. (d−f) Schematic ball-and-stick model of different SWNT growth stages.

that the carbon cap of a SWNT is stabilized by the fact that carbon precipitation is faster than the speed of step withdrawal.[10] Our data suggests that the "cap-finding" process of a SWNT involves the dynamic reshaping of the catalyst crystal itself. This is very important, as the initial cap uniquely determines the chirality of the nanotube that will grow out of it.[31] It should be noted that this holds only for hemispherical caps; for cone-shaped caps, the SWNT chirality depends on the introduction of a further pentagon. We suggest that chiral selectivity may be related dynamically to catalyst particle−carbon network interactions.

For high-temperature arc-discharge and laser ablation techniques, gas-phase-based SWNT nucleation is often observed perpendicular to the catalyst surface, with multiple SWNTs emerging from large catalyst particles.[2,32] Figure 6 shows that, at our CVD conditions, a catalyst crystal only nucleates one SWNT, whereby the metal particle size and dynamics determine the SWNT diameter (see Supporting Information video S2). Cap diameters below 0.72 nm require the formation of adjacent pentagons and have a high curvature energy.[31] Thus it is unlikely that a small, highly deformable catalyst particle can nucleate such a nanotube diameter (irrespective of structural and chemical changes for such small metal clusters). Catalyst particles larger than 2 nm were observed to have predominantly cone-shaped caps;[10] we suggest the graphitic cone reshapes the catalyst particle, and the transition to nanotube growth occurs when the cone opening matches the new catalyst dimensions. The nucleation of SWNT diameters over 5 nm requires the deformation of increasingly larger catalyst particles, whereby the surface curvature becomes unfavorable for a carbon cap lift-off. Large catalyst particles end up encapsulated with carbon, which is a common observation for CVD.[6]

It has been shown that the SWNT chirality distribution can be influenced by careful catalyst engineering.[19] The main effect of an increase in CVD temperature is typically an increase in catalyst particle size and hence larger nanotube diameter.[12,19,33] The gaseous feed composition can influence the rate of carbon deposition and thus indirectly affect the SWNT diameter based on a different catalyst island agglomeration time before the carbon cap stabilizes.[19] The detailed topography of catalyst particles depends strongly on the support and gas exposure[17] (Figure 1), and the resulting effect on chiral selectivity for a given SWNT diameter was previously discussed in terms of a matching carbon cap.[19,33] We emphasize that chiral selectivity is related to the graphitic lattice−metal dynamics, of which the initial catalyst crystal shape is only the starting point. The support influences the induced reshaping (Figure 7) and hence also the kinetics of carbon cap formation. For prolonged growth, in particular if not suspended, the SWNT body exerts an increasing moment on the growth interface that can lead to defect formation and growth interruption.

In conclusion, we have used ETEM and in situ time-resolved XPS to reveal some of the catalyst dynamics that occur during surface-bound SWNT and CNF nucleation. Selective acetylene chemisorption and the formation of a carbon-rich surface layer were observed on otherwise crystalline transition metal nanoparticles. Structural selectivity was determined by the dynamic interplay between carbon network formation and catalyst particle deformation.

**Supporting Information Available:** ETEM videos (Mpeg4) and descriptive text (PDF) of CNF tip-growth (3:1 $NH_3$:$C_2H_2$ at 1.3 mbar total pressure, 480 °C) and CNT root growth ($8 \times 10^{-3}$ mbar $C_2H_2$, 615 °C). This material is available free of charge via the Internet at http://pubs.acs.org.

## References

(1) Puretzky, A. A.; Schittenhelm, H.; Fan, X. D.; Lance, M. J.; Allard, L. F.; Geohegan, D. B. *Phys. Rev. B* **2002**, *65*, 245425.

(2) Saito, Y. *Carbon* **1995**, *33*, 979.

(3) Radushkevich, L. V.; Lukyanovich, V. M. *Z. Fis. Chim.* **1952**, *26*, 88.

(4) Hata, K.; Futaba, D. N.; Mizuno, K.; Namai, T.; Yumura, M.; Iijima, S. *Science* **2004**, *306*, 1362.

(5) Helveg, S.; Lopez-Cartes, C.; Sehested, J.; Hansen, P. L.; Clausen, B. S.; Rostrup-Nielsen, J. R.; Abild-Pedersen, F.; Norskov, J. K. *Nature* **2004**, *427*, 426.

(6) Lin, M.; Tan, J. P. Y.; Boothroyd, C.; Loh, K. P.; Tok, E. S.; Foo, Y. L. *Nano Lett.* **2006**, *6*, 449.

(7) Fan, S. S.; Liu, L.; Liu, M. *Nanotechnology* **2003**, *14*, 1118.

(8) Li, X. S.; Cao, A. Y.; Jung, Y. J.; Vajtai, R.; Ajayan, P. M. *Nano Lett.* **2005**, *5*, 1997.

(9) Zhang, Y.; Li, Y.; Kim, W.; Wang, D.; Dai, H. *Appl. Phys. A* **2002**, *74*, 325.

(10) Zhu, H. W.; Suenaga, K.; Hashimoto, A.; Urita, K.; Hata, K.; Iijima, S. *Small* **2005**, *1*, 1180.

(11) Hofmann, S.; Csanyi, G.; Ferrari, A. C.; Payne, M. C.; Robertson, J. *Phys. Rev. Lett.* **2005**, *95*, 036101.

(12) Cantoro, M.; Hofmann, S.; Pisana, S.; Scardaci, V.; Parvez, A.; Ducati, C.; Ferrari, A. C.; Blackburn, A. M.; Wang, K. Y.; Robertson, J. *Nano Lett.* **2006**, *6*, 1107.

(13) Sharma, R. *J. Mater. Res.* **2005**, *20*, 1695.

(14) Yokota, T.; Murayama, M.; Howe, J. M. *Phys. Rev. Lett.* **2003**, *91*, 265504.

(15) Mullins, W. W. *J. Appl. Phys.* **1957**, *28*, 333.

(16) Anton, R. *J. Mater. Res.* **2005**, *20*, 1837.

(17) Hansen, P. L.; Wagner, J. B.; Helveg, S.; Rostrup-Nielsen, J. R.; Clausen, B. S.; Topsoe, H. *Science* **2002**, *295*, 2053.

(18) Pisana, S.; Cantoro, M.; Parvez, A.; Hofmann, S.; Ferrari, A. C.; Robertson, J. *Physica E* **2006**, in press.

(19) Lolli, G.; Zhang, L. A.; Balzano, L.; Sakulchaicharoen, N.; Tan, Y. Q.; Resasco, D. E. *J. Phys. Chem. B* **2006**, *110*, 2108.

(20) Hofmann, S.; Cantoro, M.; Kleinsorge, B.; Casiraghi, C.; Parvez, A.; Robertson, J.; Ducati, C. *J. Appl. Phys.* **2005**, *98*, 034308.

(21) Malm, J. O.; O'Keefe, M. A. *Ultramicroscopy* **1997**, *68*, 13.

(22) Nishimura, K.; Okazaki, N.; Pan, L. J.; Nakayama, Y. *Jpn. J. Appl. Phys.* **2004**, *43*, L471.

(23) Bertoni, G.; Cepek, C.; Romanato, F.; Casari, C. S.; Bassi, A. L.; Bottani, C. E.; Sancrotti, M. *Carbon* **2004**, *42*, 440.

(24) Panzner, G.; Diekmann, W. *Surf. Sci.* **1985**, *160*, 253.

(25) Wiltner, A.; Linsmeier, C. *Phys. Status Solidi A* **2004**, *201*, 881.

(26) Lascovich, J. C.; Giorgi, R.; Scaglione, S. *Appl. Surf. Sci.* **1991**, *47*, 17.

(27) Alstrup, I. *J. Catal.* **1988**, *109*, 241.

(28) Neubauer, R.; Whelan, C. M.; Denecke, R.; Steinruck, H. P. *J. Chem. Phys.* **2003**, *119*, 1710.

(29) Jiang, A.; Awasthi, N.; Kolmogorov, A. N.; Setyawan, W.; Boerjesson, A.; Bolton, K.; Harutyunyan, A. R.; Curtarolo, S. **2006**, cond-mat/0612562.

(30) Niimi, Y.; Matsui, T.; Kambara, H.; Tagami, K.; Tsukada, M.; Fukuyama, H. *Phys. Rev. B* **2006**, 73, 085421.

(31) Reich, S.; Li, L.; Robertson, J. *Phys. Rev. B* **2005**, 72, 165423.

(32) Gavillet, J.; Loiseau, A.; Journet, C.; Willaime, F.; Ducastelle, F.; Charlier, J. C. *Phys. Rev. Lett.* **2001**, *8727*, 275504.

(33) Miyauchi, Y. H.; Chiashi, S. H.; Murakami, Y.; Hayashida, Y.; Maruyama, S. *Chem. Phys. Lett.* **2004**, *387*, 198.